Check for updates

View Article Online
View Journal

Catalysis Science & Technology

Accepted Manuscript

This article can be cited before page numbers have been issued, to do this please use: B. Aljaman, S. Komaty, N. M. Alghamdi, C. Kalamaras, S. M. Sarathy and J. Ruiz Martinez, *Catal. Sci. Technol.*, 2026, DOI: 10.1039/D6CY00260A.

This is an Accepted Manuscript, which has been through the Royal Society of Chemistry peer review process and has been accepted for publication.

Accepted Manuscripts are published online shortly after acceptance, before technical editing, formatting and proof reading. Using this free service, authors can make their results available to the community, in citable form, before we publish the edited article. We will replace this Accepted Manuscript with the edited and formatted Advance Article as soon as it is available.

You can find more information about Accepted Manuscripts in the Information for Authors.

Please note that technical editing may introduce minor changes to the text and/or graphics, which may alter content. The journal's standard Terms & Conditions and the Ethical guidelines still apply. In no event shall the Royal Society of Chemistry be held responsible for any errors or omissions in this Accepted Manuscript or any consequences arising from the use of any information it contains.

ROYAL SOCIETY OF CHEMISTRY

rsc.li/catalysis

View Article Online
DOI: 10.1039/D6CY00260A

ARTICLE

Performance evaluation of Pt and Pd mono- and bi-metallic H_2-SCR catalysts for NO emission control applications

Received 00th January 20xx,
Accepted 00th January 20xx

DOI: 10.1039/x0xx00000x

Baqer Aljaman[a], Sarah Komaty[a], Nawaf M. Alghamdi[b], Christos Kalamaras[b], S. Mani Sarathy[a], and Javier Ruiz-Martinez*[a]

Hydrogen-based selective catalytic reduction (H_2-SCR) offers a promising pathway for mitigating NOx emissions, particularly in hydrogen internal combustion engine (H_2-ICE) applications. This study investigates how noble-metal identity and Pd–Pt interactions influence the H_2-SCR of NO over CeO_2–ZrO_2-supported catalysts. The monometallic catalysts show that Pd achieves catalytic activity comparable to Pt while providing higher N_2 selectivity, indicating a more favourable balance between hydrogen activation and selective NO reduction. Incorporation of both metals modifies this activity–selectivity relationship. Comparison with a physical mixture of the corresponding monometallic catalysts shows that simple coexistence of Pd- and Pt-containing particles does not reproduce the behaviour of the co-impregnated bimetallic catalyst. H_2-TPR reveals modified reduction behaviour in the bimetallic system, while CO-DRIFTS shows changes in the CO adsorption environment of Pd-containing surface sites in the presence of Pt. Collectively, these findings support the presence of modified Pd/Pt surface environments, potentially involving close Pd–Pt proximity or interfacial interaction, which govern hydrogen utilization and the NO conversion–N_2 selectivity balance during H_2-SCR.

Introduction

Headings 50 billion tons of GHGs are emitted on a yearly basis, contributing to global warming and environmental degradation [1]. In response, regulatory frameworks have become more stringent to minimize the impact of GHGs emissions and accelerate the energy transition [2]. Therefore, substantial technological and infrastructural efforts are required to meet this target, particularly in sectors with high carbon intensity.

Around 24% of global CO_2 emissions are produced by the transportation sector, which rely heavily on fossil fuels [3]. The use of electric powertrains is a promising pathway for decarbonization; however, areas with limited access to charging stations, heavy-duty vehicles and long-distance travel represent key challenges [4,5]. A promising alternative is the hydrogen internal combustion engine (H_2-ICE), which is carbon-free and can be achieved with minimal modifications to existing engines [6]. However, the high temperature of H_2 combustion results in the formation of nitrogen oxides (NOx), including nitric oxide (NO), nitrogen dioxide (NO_2) and nitrous oxide (N_2O). They are considered a major health concern to humans and the environment due to their ability to damage the respiratory system and cause cardiovascular disease, as well as their contribution to acid rain and ground-level ozone [7].

Selective catalytic reduction (SCR) is an efficient NOx emission treatment technology, and several reducing agents have been investigated, including ammonia (NH_3-SCR) [8–10], hydrocarbons (HC-SCR) [11–13], and hydrogen (H_2-SCR) [14–17]. Among these, NH_3-SCR is widely employed in the transportation sector. Despite its potential, NH_3-SCR faces several challenges, such as ammonia slip, air heater fouling, and reduced performance during startup, partly due to its effectiveness at high-temperatures. In the context of H_2-ICE, H_2 can also be utilized as environmentally-friendly and low temperature reductant, to selectively convert NOx into nitrogen (N_2) and water (H_2O) in the presence of oxygen (O_2). However, minimizing NOx emissions from H_2-ICE requires a high-performing aftertreatment system that can sustain both high NO conversion and N_2 selectivity under a wide range of operating conditions to satisfy the stringent emission regulations. Therefore, the development of a robust and reliable H_2-SCR system, capable of efficient operation across various operating conditions, is critical.

Noble metals, particularly Pt and Pd, supported on oxide or zeolitic materials have been widely investigated for H_2-SCR because of their ability to activate H_2 and promote NOx reduction under lean conditions [18–20]. Recent studies have shown that the identity of the noble metal strongly affects the temperature window and product

[a] King Abdullah University of Science and Technology (KAUST), Thuwal 23955-6900, Saudi Arabia.
[b] Sustainable Transport Technologies R&D Division, Research & Development Center, Saudi Aramco, Dhahran, Saudi Arabia 31311
* E-mail: Javier.ruizmartinez@kaust.edu.sa

Open Access Article. Published on 08 June 2026. Downloaded on 6/8/2026 11:29:15 PM.
This article is licensed under a Creative Commons Attribution 3.0 Unported Licence.

Catalysis Science & Technology Accepted Manuscript

View Article Online
DOI: 10.1039/D6CY00268A

Open Access Article. Published on 08 June 2026. Downloaded on 6/8/2026 11:29:15 PM. This article is licensed under a Creative Commons Attribution 3.0 Unported Licence.

Catalysis Science & Technology Accepted Manuscript

selectivity. Shao et al. compared Pt-, Pd-, and Ir-based SSZ-13 catalysts and showed that these metals exhibit different effective temperature ranges in H_2-SCR, while combining noble-metal functions can broaden the overall operating window for NO reduction by H_2 [21]. This highlights the importance of noble-metal selection and motivates further comparison of Pt- and Pd-based catalysts under relevant H_2-SCR conditions.

In addition to the active metal, the catalytic performance is strongly influenced by the support and by the strength of the metal–support interaction. Recent work on Pt-based H_2-SCR catalysts has shown that support identity, promoter chemistry, metal loading, pretreatment, space velocity, and feed composition can significantly alter NOx conversion, H_2 activation, and N_2 selectivity [22]. Maurer et al. demonstrated that Pt nanoparticles on suitable oxide supports are essential for low-temperature NOx conversion, while support acidity/basicity and promoter addition can shift or broaden the activity and selectivity windows [23]. Similarly, Li et al. reported that Zr modification of Pt/TiO_2 enhances NOx conversion and N_2 selectivity in a wider low-temperature range, showing that tuning the support composition can regulate Pt electronic state, adsorption behaviour, and the balance between NOx reduction and competitive H_2 oxidation [20].

Among oxide supports, CeO_2–ZrO_2 mixed oxides are particularly attractive because they combine the redox properties of ceria with the enhanced oxygen mobility and thermal stability provided by zirconia [24]. The reversible Ce^{3+}/Ce^{4+} redox cycle can influence oxygen vacancy formation, NOx adsorption, and surface oxygen mobility, while Zr incorporation improves the structural and redox stability of ceria-based materials [25]. For instance, CeO_2-based Pd catalysts investigated by Patel and Sharma showed improved H_2-SCR performance upon ZrO_2 addition, which was associated with changes in Ce^{3+}/Ce^{4+} ratio and oxygen-related surface properties [24]. Kalamaras et al. also reported that $Pt/Ce_xZr_{1-x}O_{2-\delta}$ catalysts are active for NO reduction using H_2 and C_3H_6 as reducing agents, with $Pt/Ce_{0.5}Zr_{0.5}O_2$ showing the highest NO conversion [26].

Bimetallic systems have attracted increasing attention because combining two metals can modify hydrogen activation, NOx adsorption, and reaction selectivity beyond what is achieved with monometallic catalysts. Au addition to Pd/TiO_2 has been reported to improve NO conversion, while Co promotion of Pd/TiO_2 enhanced both NO conversion and N_2 selectivity through modified reaction pathways involving H_2 activation and adsorbed nitrogen-containing intermediates [27,28]. These findings suggest that metal–metal interactions, together with the support environment, can play a decisive role in controlling the activity–selectivity balance in H_2-SCR. Therefore, investigating bimetallic interactions on CeO_2–ZrO_2 is a promising approach for understanding how metal identity, metal–metal interaction, and support redox properties collectively control the activity–selectivity balance in H_2-SCR.

In this work, we investigated the effect of bimetallic systems supported on CZ on NOx reduction using H_2. Pd-Pt catalysts with varying metal compositions (Pd/CZ, 0.7Pd-0.3Pt/CZ, 0.5Pd-0.5Pt/CZ, 0.3Pd-0.7Pt/CZ, Pt/CZ) were prepared to investigate how the interaction of Pd and Pt influences catalytic performance of H_2-SCR.

Experimental

Catalyst preparation

An aqueous solution of 2.5 g cerium (III) nitrate hexahydrate [$Ce(NO_3)_3$] (Sigma Aldrich) and 3.5 g Zirconyl(IV) nitrate hydrate [$ZrO(NO_3)_2xH_2O$] (Thermo Scientific) was prepared by dissolving the salts in deionized water and stirred for 2 h at room temperature. A [19,29]separate recipient containing 20 mL of ammonium hydroxide (NH_4OH, pH=10.5) was used for co-precipitation. The mixed metal nitrate solution was loaded into a syringe pump and injected simultaneously with NH_4OH (Sigma-Aldrich, 97%) into the vessels using a Gilson pump under continuous stirring. During the co-injection, the formation of brownish/yellowish precipitates was observed. The resulting precipitates were stirred for an additional 30 min at 450 rpm, then separated by centrifugation at 7500 rpm for 7 min. The precipitate was washed three times with deionized water, with 10 min of sonication between each wash. The cleaned precipitate was dried at 100 °C overnight, ground into a fine powder, and then calcined at 500 °C for 6 h at a heating rate of 2 °C min^{-1}, resulting in final composition of 50 wt% of each metal oxide. This co-precipitation method ensures homogenous and well-mixed oxides formation by maintaining a constant pH during the synthesis [18].

The active metal was introduced into the oxide support using the conventional incipient wetness impregnation method. 17.2 mg of Palladium (II) Chloride ($PdCl_2$) (Alfa Aesar) and 29.7 mg of Sodium hexachloroplatinate (IV) (Na_2PtCl_6) (Thermo Fisher Scientific) were dissolved in a mixture of deionized water and hydrochloric acid (HCl) for Pd/CZ and Pt/CZ, respectively. For bi
metallic catalysts, an appropriate amount of Pd and Pt precursors were dissolved corresponding to each Pd/Pt ratio. The resulting solution was added dropwise onto the oxide support under continuous stirring to ensure uniform metal dispersion. The impregnated samples were freeze-dried overnight to remove moisture. The synthesized catalysts have a total metal loading of 0.5 wt% and are denoted as Pd/CZ, 0.7Pd–0.3Pt/CZ, 0.5Pd–0.5Pt/CZ, 0.3Pd–0.7Pt/CZ, and Pt/CZ, reflecting their respective mass Pd/Pt compositions. Additionally, a physical mixture of 0.5%Pd/CZ and 0.5%Pt/CZ was prepared by mechanically mixing the corresponding monometallic catalysts to compare with the impregnated 0.5Pd-0.5Pt/CZ catalyst.

Catalysts characterization

Nitrogen physisorption was used to determine the specific surface area, pore volume, and pore size distribution of the samples using an ASAP 2420 surface area and porosity analyzer (Micromeritics). Prior to measurement, all samples were degassed at 350 °C for 4 h using a heating rate of 10 °C min^{-1}. The Brunauer–Emmett–Teller (BET) method was utilized to calculate the specific surface area over a relative pressure range (P/P_o) of 0.05–0.30. The pore volume and pore size distribution were determined using the Barrett–Joyner–Halenda (BJH) method.

This journal is © The Royal Society of Chemistry 2026

Please do not adjust margins

View Article Online
DOI: 10.1039/D5CY00268A

Open Access Article. Published on 08 June 2026. Downloaded on 6/8/2026 11:29:15 PM. This article is licensed under a Creative Commons Attribution 3.0 Unported Licence.

Catalysis Science & Technology Accepted Manuscript

X-ray diffraction (XRD) analysis was performed using a Bruker D8 Advance diffractometer equipped with a Cu Kα radiation source (λ = 0.15406 nm). The measurements were conducted over a 2θ range of 10–90°, with a scanning rate of 5° min^{-1} and a step size of 0.02°.

H_2 temperature-programmed reduction (H_2-TPR) was used to investigate the effect of platinum group metal addition on the reduction behaviour of the catalysts, using an AutoChem II Chemisorption Analyzer (Micromeritics) equipped with a thermal conductivity detector (TCD). Prior to analysis, 0.1 g of catalyst was pretreated under He flow (50 mL min^{-1}) at 350 °C for 1 h, followed by cooling to 35 °C. A gas mixture of 10% H_2/Ar (50 mL min^{-1}) was then introduced, and the temperature was increased to 700 °C at a heating rate of 10 °C min^{-1}.

CO diffuse reflectance infrared Fourier transform spectroscopy (CO-DRIFTS) measurements were performed to investigate the nature of the accessible surface metal sites. Prior to CO adsorption, the catalyst was treated under N_2 flow (50 mL min^{-1}) at 300 °C for 1 h using a heating rate of 10 °C min^{-1}. The sample was then reduced under 6% H_2/Ar flow (50 mL min^{-1}) at 300 °C for 45 min, followed by purging with N_2 at the same temperature for 45 min. Subsequently, the sample was cooled to room temperature under N_2 flow, and a background spectrum was recorded. CO adsorption was carried out by exposing the catalyst to 3% CO/N_2 (30 mL min^{-1}) for 45 min. After adsorption, the sample was purged with N_2 (50 mL min^{-1}) for 45m min to remove weakly adsorbed and gas-phase CO species, after which the DRIFTS spectrum was collected.

CO chemisorption was carried out using 0.1 g of catalyst in an AutoChem III Chemisorption Analyzer (Micromeritics) coupled with a TCD. Prior to CO pulse adsorption, the catalyst was reduced under 10% H_2/Ar flow (75 mL min^{-1}) at 225 °C for 30 min, followed by cooling to 35 °C. CO pulse injections were then performed using 10% CO/He at a flow rate of 75 mL min^{-1} until saturation was reached. For the monometallic Pd/CZ and Pt/CZ catalysts, metal dispersion and average particle size were determined based on the amount of chemisorbed CO, assuming metal-to-CO stoichiometric ratios (M/CO) of 2.0 and 1.0 for Pd/CZ and Pt/CZ, respectively. Quantitative metal dispersion and particle size were not determined for the bimetallic catalysts because the CO adsorption stoichiometry cannot be reliably assigned for mixed Pd–Pt surface sites. Metal dispersion was calculated using the following equation:

$$\text{Dispersion } (\%) = \frac{V_m W_a F_s}{V_{mol}\, M_{loading}} \times 100\% \qquad (1)$$

Where V_m is cumulative quantity ($cm^3\ g^{-1}$ STP), W_a is metal molar mass (g mol^{-1}), F_s is M/CO ratio, V_{mol} is standard molar volume ($cm^3\ mol^{-1}$) and $M_{loading}$ is the total metal loading.

The metal loading and support composition were determined using inductively coupled plasma optical emission spectroscopy (ICP-OES). Transmission electron microscopy (TEM) and TEM-energy-dispersive X-ray spectroscopy (TEM-EDX) were employed as complementary techniques to examine the catalyst morphology and detect the supported noble-metal elements using a Titan 60–300 instrument (FEI Co., Netherlands). High-resolution X-ray photoelectron spectroscopy (XPS) was performed using an Axis Ultra spectrometer to investigate the surface chemical states. The resulting spectra were further analyzed by peak fitting using CasaXPS software.

Catalytic activity measurements

H_2-SCR catalytic activity measurements were conducted in a quartz packed-bed reactor with an internal diameter of 10 mm, operated at atmospheric pressure over a temperature range of 150-450 °C. In each experiment, the reactor was loaded with 250 mg of catalyst (35-60 mesh) positioned between two layers of quartz wool. The total flow rate of the reaction feed was maintained at 100 mL min^{-1}, corresponding to a gas hourly space velocity (GHSV) of 50,000 h^{-1}. The feed composition consisted of 450 ppm NO, 0.5% H_2, 2.5% O_2, and balance N_2. The H_2-SCR experiments were conducted using a Microactivity Reference system from PID Eng&Tech. The PID system includes an internal thermocouple for temperature monitoring, and Bronkhorst mass flow controllers (MFCs) connected to the PID system for precise control of the reaction conditions. Reactants and products were analyzed using MultiGas™ 2030 FTIR Gas Analyzers (MKS) and TRACE™ 1600 Series Gas Chromatograph (Thermo Fisher Scientific). The FTIR was employed for the analysis of NO, NO_2, N_2O, NH_3, and H_2O, while the GC was used to quantify H_2, and O_2. N_2 selectivity was calculated using Equation 3 based on the outlet concentrations of NO, NO_2, N_2O, and NH_3 measured by FTIR. Prior to each H_2-SCR measurement, the catalyst was pretreated in a N_2 flow of 200 mL min^{-1} for 2 h at 450 °C, followed by a reduction step of 20 mL min^{-1} of 4% H_2/N_2 gas flow for 1h at 225 °C. The NO conversion, N_2 selectivity and H_2 conversion were calculated as follows:

$$\text{NO conversion} = \frac{[NO]_{in} - [NO]_{out}}{[NO]_{in}} \times 100\% \qquad (2)$$

$$N_2 \text{ selectivity} = \frac{[NO]_{in} - [NO]_{out} - [NO_2]_{out} - 2\times[N_2O]_{out} - [NH_3]_{out}}{[NO]_{in} - [NO]_{out}} \times 100\% \qquad (3)$$

$$H_2 \text{ conversion} = \frac{[H_2]_{in} - [H_2]_{out}}{[H_2]_{in}} \times 100\% \qquad (4)$$

Results and discussion

Catalytic activity measurements

Figure 1 shows the NO conversion (Figure 1a) and N_2 selectivity (Figure 1b) for Pd/CZ, 0.7Pd-0.3Pt/CZ, 0.5Pd-0.5Pt/CZ, 0.3Pd-0.7Pt/CZ, and Pt/CZ catalysts in the 150-450 °C range at a GHSV of 50,000 h^{-1}. Pt/CZ exhibits superior NO conversion of over 92% in the low temperature range (150-200 °C) with a maximum NO conversion of 98% at 175 °C. This correlates with the H_2 conversion shown in Figure 1c, suggesting that Pt/CZ exhibits strong H_2 activation below 200 °C, which contributes directly to the high NO reduction efficiency under these conditions. However, its catalytic activity drops above 200 °C, most likely due to the complete depletion of H_2 by the unselective oxidation with O_2. Pt/CZ also exhibits a significant decline in N_2 selectivity at low temperature, dropping to 45% at 200 °C, despite achieving complete H_2 conversion.

In contrast, Pd/CZ maintains excellent NO conversion of over 80% in the range of 150-250 °C and relatively high N_2 selectivity. A comparison between the temperatures of peak NO conversion and the onset of full H_2 conversion reveals that the decline in NO conversion at higher temperatures is due to increased competitive

Please do not adjust margins

View Article Online
DOI: 10.1039/D6CY00260A

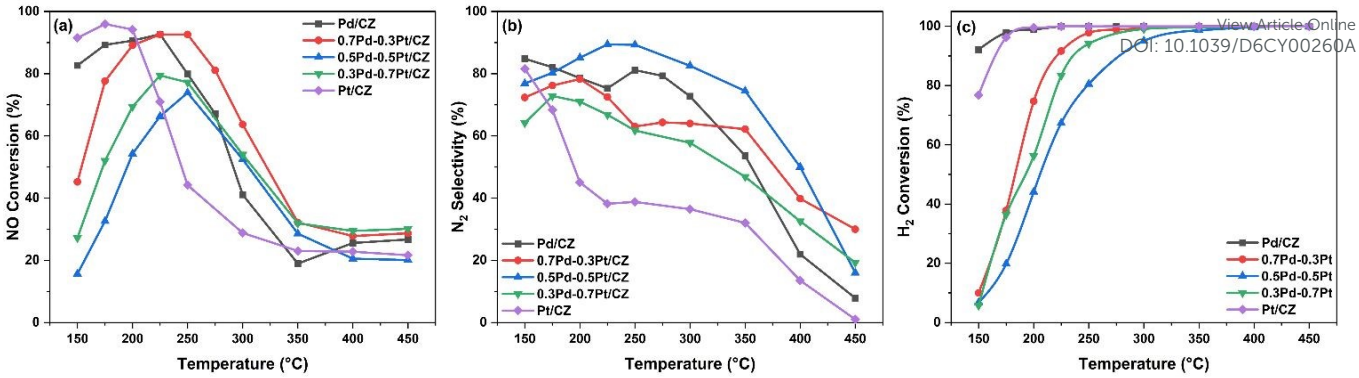

Figure 1: (a) NO conversion, (b) N_2 selectivity and (c) H_2 conversion over xPd-(1-x)Pt/CZ catalysts, where x=0-1. Reaction conditions: 450 ppm NO, 0.5%H_2, 2.5% O_2, balance N_2, total flow rate=100 mL min^{-1}, GHSV=50,000 1/h

H_2 combustion, which consumes the reducing agent (H_2) needed for the H_2-SCR reaction.

On the other hand, bimetallic catalysts display a different trend, with Gaussian-shaped NO conversion profiles peaking in the 200–250 °C range. Among them, 0.7Pd–0.3Pt/CZ shows the highest NO conversion with roughly 80% in the 175–275 °C range. Bimetallic catalysts also present high overall N_2 selectivity, with the 0.5Pd-0.5Pt/CZ sample showing the best performance, maintaining over 75% N_2 selectivity between 150-350 °C. All catalysts exhibit a decline in both NO conversion and N_2 selectivity at higher temperatures. This decrease is attributed to the depletion of available H_2 due to its preferential reaction with oxygen, leading to the formation of H_2O rather than N_2. At elevated temperatures, H_2 depletion leads to NO_2 formation originating from NO oxidation as it can be seen in Figure S1b. Interestingly, complete H_2 consumption over the monometallic catalysts begins at temperatures 100-150 °C lower than those observed for their bimetallic counterparts. This shift indicates that the existence of a Pt-Pd system delays H_2 oxidation, suggesting a synergistic interaction between the two noble metals that modifies the surface properties and redox behaviour of the catalyst [27].

Considering the distinct catalytic behaviour of the Pd–Pt-containing catalysts, we further examined whether the simultaneous presence of Pd and Pt in separate catalyst particles could reproduce the performance of the co-impregnated bimetallic catalyst. For this purpose, a physical mixture of the same mass of 0.5 wt% Pd/CZ and 0.5 wt% Pt/CZ was tested alongside the co-impregnated 0.5Pd–0.5Pt/CZ catalyst under identical reaction conditions (Figure 2). However, the physical mixture exhibits conversion and selectivity profiles that differ from those of the individual monometallic catalysts, indicating that the coexistence of Pd- and Pt-containing particles influences the overall H_2-SCR behaviour.

This observation prompted further investigation of whether co-impregnation alters the reduction behaviour, oxidation state and surface adsorption properties of the noble-metal species. Accordingly, various characterization analyses, including H_2-TPR and CO-DRIFTS, were used to probe the differences between the physical mixture and the co-impregnated Pd–Pt/CZ catalyst and to obtain further insight into the nature of the Pd–Pt interaction.

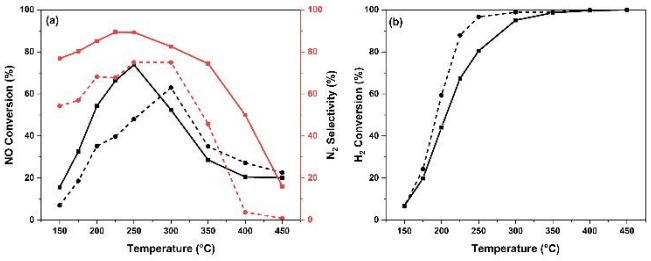

Figure 2: (a) NO conversion and N_2 selectivity and (b) H_2 conversion over 0.5Pd-0.5Pt/CZ catalyst and physical mixture of 0.5%Pd/CZ and 0.5%Pt/CZ. Reaction conditions: 450 ppm NO, 0.5%H_2, 2.5% O_2, balance N_2, total flow rate=100 mL min^{-1}, GHSV=50,000 h^{-1}. Square solid line represents the impregnated 0.5%(0.5Pd-0.5Pt)/CZ catalyst and circle dash line presents the physical mixture of 0.5%Pd/CZ and 0.5%Pt/CZ catalyst. Black and red line in (a) represents NO conversion and N_2 selectivity, respectively.

Textural properties

Table 1 summarizes the textural properties of the mesoporous catalysts, including BET surface area (56–79 m^2/g), pore volume (0.058–0.074 cm^3/g,) and pore diameter (3.7–4.3 nm). All catalysts exhibit type IV isotherms with N_2 adsorption–desorption hysteresis loops, consistent with mesoporous structures according to IUPAC classifications [30]. The N_2 adsorption–desorption isotherm of CeO_2-ZrO_2 support remains unchanged after the introduction of Pd and Pt via impregnation, suggesting that the mesostructure is preserved. This finding, further supported by XRD results in Figure 3, confirms that the structural integrity is maintained, ensuring a reliable basis for comparison among the catalysts.

All catalysts display mesoporous structures (D_P = 3.7–4.3 nm), typical of $CeZrO_x$-based materials [26,31]. The monometallic catalysts have exhibit relatively higher BET surface area (70-79 m^2/g) compared to the bimetallic ones (56-66 m^2/g), likely due to partial pore blockage by the metal nanoparticles. All catalysts exhibit close textural properties including surface area, pore size, and pore volume. As a result, the variations observed in the catalytic performance cannot be ascribed to differences in diffusional properties.

Open Access Article. Published on 08 June 2026. Downloaded on 6/8/2026 11:29:15 PM.
This article is licensed under a Creative Commons Attribution 3.0 Unported Licence.

Catalysis Science & Technology Accepted Manuscript

This journal is © The Royal Society of Chemistry 2026

Please do not adjust margins

View Article Online
DOI: 10.1039/D6CY00860A

Open Access Article. Published on 08 June 2026. Downloaded on 6/8/2026 11:29:15 PM.
This article is licensed under a Creative Commons Attribution 3.0 Unported Licence.

Catalysis Science & Technology Accepted Manuscript

Table 1: Textural properties of xPd-(1-x)Pt/CZ catalysts, where x=0-1

Catalyst	S_{BET} ($m^2 g^{-1}$)	V_p ($cm^3 g^{-1}$)	D_P (nm)
Pd/CZ	70	0.069	3.77
0.7Pd-0.3Pt/CZ	66	0.059	3.69
0.5Pd-0.5Pt/CZ	56	0.061	4.26
0.3Pd-0.7Pt/CZ	56	0.058	3.93
Pt/CZ	79	0.074	3.72
CZ	74	0.063	3.53

Figure 3 shows the XRD patterns for CeO_2, ZrO_2, CZ, and xPd-(1−x)Pt/CZ catalysts (where x=0–1). No distinct ZrO_2 diffraction peaks are observed, suggesting successful incorporation into the ceria framework to form a solid solution. All samples display a single cubic CeO_2-ZrO_2 crystalline phase consistent with the standard reference (PDF #04-005-9597) [32]. The main diffraction peaks of crystal structure (CeO_2) appear at 2θ = 28.5°, 33.1°, 47.6°, 56.4°, and 69.4° corresponding to (111), (200), (220), (311), (400), and (420) planes, respectively. In contrast, the peaks for the CeO_2-ZrO_2 solid solution are slightly shifted to higher angles (2θ = 29.6°, 34.0°, 49.1°, 58.5° and 70.9°), indicating the successful incorporation of Zr^{4+} into the CeO_2 lattice. This shift is attributed to the smaller ionic radius of Zr^{4+} (0.84 Å) compared to Ce^{4+} (0.97 Å) [24]. No diffraction peaks corresponding to Pd or Pt are detected, likely due to the low metal loading or high dispersion of these metals.

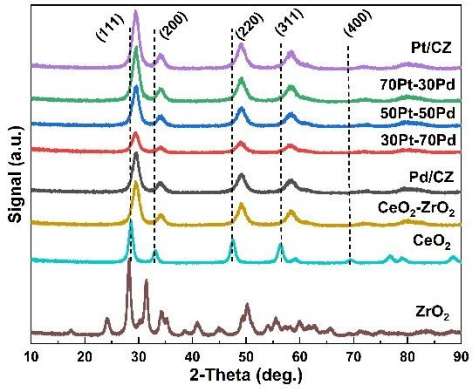

Figure 3: XRD patterns for CeO_2, ZrO_2 and xPd-(1-x)Pt/CZ catalysts, where x=0-1

The influence of redox property is investigated by H_2-TPR experiments, and the resulting reduction profiles are presented in Figure 4. For all metal loaded CZ catalysts, a single main hydrogen consumption is consistently observed and attributed to the reduction of palladium oxides (PdO_x) and/or platinum oxides (PtO_x) species interacting with the CZ support [24,33].

The presence of a single hydrogen consumption contribution in all bimetallic catalysts suggests an interaction between Pd and Pt species. This interaction likely facilitates the H_2 spillover phenomenon, where Pd acts as the primary site for H_2 dissociation, and the resulting hydrogen could migrate to adjacent Pt sites, enabling the reduction of the catalysts' metals at lower temperature. In other words, this cooperative effect results in a unified reduction event indicating interaction between Pd and Pt metals [34].

The H_2-TPR reduction temperature increases with higher Pt/Pd ratio, ranging from 115 °C for Pd/CZ to 240 °C for the Pt-only/CZ catalyst. This trend is attributed to the stronger Pt-O-Ce/Zr bonds, which stabilize oxidized Pt species and make them more resistant to reduction. Table 2 summarizes the H_2 uptake for each catalyst, showing a general increase in H_2 consumption with increasing Pt content. The Pt/CZ sample exhibits the highest H_2 uptake, indicating greater oxidation state of the Pt species. A broad contribution appears at around 545 °C, corresponding to the surface reduction of Ce^{4+} to Ce^{3+} in the $CeZrO_x$ support. For the Pd- and Pt-loaded CZ catalysts, this reduction peak shifts to around 500 °C, indicating that the presence of noble metals facilitates the surface reduction of the ceria–zirconia support [35,36].

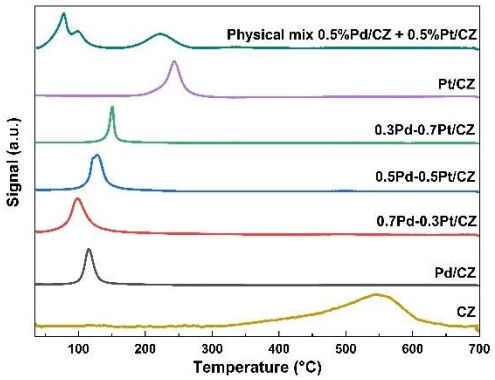

Figure 4: H_2-TPR profiles of CZ, xPd-(1-x)Pt/CZ catalysts (where x=0-1) and physical mixture of Pd/CZ and Pt/CZ

Table 2: H_2-uptake using H_2-TPR, and metal dispersion and particle size by CO-Chemisorption over xPd-(1-x)Pt/CZ catalysts, where x=0-1

Catalyst	H_2-TPR		CO-Chemisorption	
	Temperature at maximum (°C)	Exp. H_2 quantity (mmol/g)	Metal dispersion (%)	Particle size (nm)
Pd/CZ	115	0.16	67	1.6
0.7Pd-0.3Pt/CZ	98	0.15	-	-
0.5Pd-0.5Pt/CZ	128	0.18	-	-
0.3Pd-0.7Pt/CZ	151	0.19	-	-
Pt/CZ	243	0.71	54	2.0

To further investigate the interaction of Pt and Pd in the bimetallic system, a H_2-TPR of the physically mixed Pd/CZ and Pt/CZ samples was performed. In contrast to the bimetallic systems, the physical mixture of Pd/CZ and Pt/CZ exhibits a distinctly different H_2-TPR profile. There are two H_2 consumption events at low temperature

Please do not adjust margins

View Article Online
DOI: 10.1039/D6CY00260A

Open Access Article. Published on 08 June 2026. Downloaded on 6/8/2026 11:29:15 PM.
This article is licensed under a Creative Commons Attribution 3.0 Unported Licence.

Catalysis Science & Technology Accepted Manuscript

and another one at higher, corresponding to the reduction of Pd and Pt, respectively. The presence of multiple, separated reduction peaks suggests that Pd and Pt species have a lower interaction compared to the bimetallic samples.

The cumulative amount of CO adsorbed during pulse chemisorption measurements was used to determine the metal dispersion and average particle size of the catalysts. For the monometallic samples, metal:CO stochiometic ratios (M:CO) of 2:1 for Pd/CZ and 1:1 for Pt/CZ were assumed, in accordance with literature reports for Pd and Pt surfaces [37,38]. Based on these assumptions, both monometallic catalysts exhibit high metal dispersion, which is consistent with their high catalytic performance in the H_2-SCR reaction. An accurate determination of metal dispersion and average particle size in these bimetallic systems is complicated by the coexistence of two metals with potentially different CO adsorption behaviour and surface compositions.

Figure 5 shows CO-DRIFTS for Pd/CZ, 0.5Pd-0.5Pt/CZ and Pt/CZ which was performed to obtain qualitative insight into the surface metal sites and the interaction between Pt and Pd species. The spectra of Pt/CZ show an intense band at 2059 cm^{-1} with shoulders at 2075 and 2019 cm^{-1}, which can be assigned to linearly adsorbed CO on Pt sites [39,40]. In contrast, Pd/CZ exhibits a weaker linear CO band at 2042 cm^{-1} together with pronounced lower-frequency bands at 1945, 1861, and 1772 cm^{-1}, characteristic of bridged and multi-coordinated CO adsorbed on Pd ensembles [41].

The presence of these intense low-frequency features indicates that Pd/CZ contains contiguous Pd surface sites accessible for multi-coordinated CO adsorption. The Pd–Pt/CZ catalyst displays a distinct CO adsorption profile compared with both monometallic catalysts. A Pt-like linear CO band is observed at 2059 cm^{-1}, while the Pd-related bridged CO region is substantially modified, showing broader and weaker features around 1882 and 1828 cm^{-1} [41]. This change suggests that the bimetallic catalyst does not behave as a simple combination of isolated Pd and Pt sites. Instead, the and lower intensity and shift of Pd-like bridged CO features are consistent with modification of the Pd surface environment, possibly through Pd ensemble dilution, electronic interaction with Pt, or formation of Pt–Pd interfacial sites. Thus, these CO-DRIFTS results should be interpreted as evidence of Pt–Pd interaction. Additional bands at 1628, 1587, and 1428 cm^{-1} are attributed to carbonate/carboxylate-type species associated with CO interaction with the CeZrOx support or metal–support interfacial oxygen species [42,43].

TEM and TEM-EDX analyses were conducted to further examine the metal distribution on the support. Although Pd and Pt signals were clearly detected in the EDX spectra, indicating metal incoorporation, no distinct metal nanoparticles were observed in the TEM images. The absence of visible particles is most likely attributed to the low metal loading (0.5 wt%), which reduces the contrast between the metallic phase and the ceria-zirconia support.

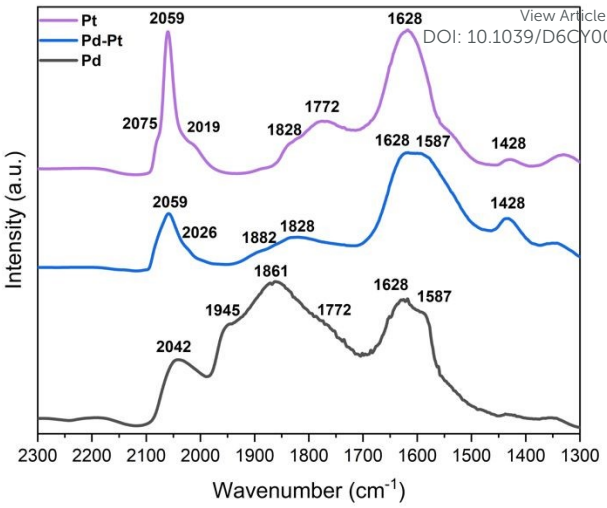

Figure 5: CO-DRIFTS of Pd/CZ, 0.5Pd-0.5Pt/CZ and Pt/CZ

Therefore, direct visualization of the metallic phase under standard imaging conditions remains challenging. The corresponding TEM images and EDX spectra are provided in Figure S2-11 in the Supplementary Information.

The surface chemical state of selected synthesized catalysts after calcination was investigated using XPS. Figure 6a shows the Ce 3d core level XPS spectra for all fresh catalysts. Eight distinct peaks are observed, representing two different spin-orbit components which represent Ce $3d_{3/2}$ and Ce $3d_{5/2}$ [44–46]. The peaks at 884.5 and 902.3 eV are assigned to Ce^{3+} species, while the peaks at 882.1, 889.2, 898.2, 900.7, 907.3, and 916.5 eV are attributed to Ce^{4+} [44,47].

The deconvolution of the XPS spectra peaks confirm the coexistence of both Ce^{3+} and Ce^{4+} oxidation states in the CeO_2-based catalysts. The relative Ce^{3+} content was quantified by calculating the area of Ce^{3+} peaks to the total Ce 3d peak area. The Ce^{3+} concentrations were found to be 32% for Pd/CZ, 24% for 0.5Pd–0.5Pt/CZ, and 35% for Pt/CZ catalysts. Notably, the fraction of Ce^{3+} in Pt/CZ and Pd/CZ sample is relatively higher compared to 0.5Pd-0.5Pt/CZ sample which correlates with the enhanced NO conversion.

Figure 6b displays the O 1s spectra for all fresh catalysts, deconvoluted into two peaks representing lattice oxygen (O_β) at 529.4 eV and surface-adsorbed oxygen (O_α) at 531.0 eV [45]. The relative proportion of surface oxygen, expressed as $O_\alpha/(O_\beta+O_\alpha)$, follows the trend Pt/CZ > Pd/CZ > 0.5Pd-0.5Pt/CZ, as summarized in Table 3.

Oxygen vacancies play a crucial role in de-NOx performance by enhancing oxygen mobility within the catalyst system which reflects the catalytic performance trend of the Pd/CZ, 0.5Pd-0.5Pt/CZ and Pt/CZ [48,49]. The Ce^{3+} content is well-correlated with the presence of surface oxygen which are favourable for the adsorption and activation of oxygen species [24].

This journal is © The Royal Society of Chemistry 2026

Please do not adjust margins

View Article Online
DOI: 10.1039/D6CY00260A

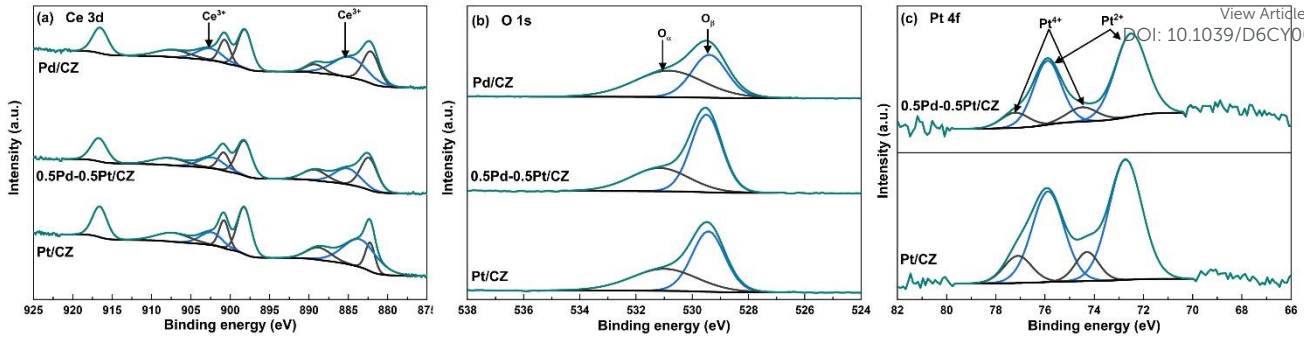

Figure 6: XPS spectra of (a) Ce 3d, (b) O 1s and (c) Pt 4f over Pd/CZ, 0.5Pd-0.5Pt/CZ and Pt/CZ

The Pt 4f XPS spectra of both 0.5Pd–0.5Pt/CZ and Pt/CZ catalysts show oxidized Pt species, namely Pt^{2+} and Pt^{4+}, which is consistent with the fact that the samples were not subjected to any pre-reduction treatment prior to analysis. The Pt $4f_{7/2}$ and Pt $4f_{5/2}$ peaks appear at 72.5 eV and 75.9 eV representing Pt^{2+} while The Pt $4f_{7/2}$ and Pt $4f_{5/2}$ peaks appear at 74.5 eV and 77.2 eV representing Pt^{4+}. These binding energies match reported values for Pt^{2+} and Pt^{4+} [50,51], confirming the presence of oxidized platinum on the catalyst surface. The shift in Pt 4f binding energies between Pt/CZ and Pd–Pt/CZ correspond to changes in Pt's electronic structure induced by Pd. This shift in binding energy evidences an electronic interaction between Pd and Pt, leading to redistribution of electron density on Pt [52].

Notably, the $Pt^{2+}/(Pt^{2+} + Pt^{4+})$ ratio in Figure 6c is similar for both catalysts, indicating that the overall oxidation state distribution of platinum on the surface remains essentially unchanged in the bimetallic catalyst. Therefore, based strictly on the XPS results, both catalysts present comparable surface populations of Pt^{2+} and Pt^{4+} species, with no evidence of metallic Pt^0 under the analysed conditions.

Table 3: The relative surface concentration of Ce^{3+}, O_α and Pt^{2+} from XPS results

Catalyst	$Ce^{3+}/(Ce^{3+}+Ce^{4+})$ (%)	$O_\alpha/(O_\alpha+O_\beta)$ (%)	$Pt^{2+}/(Pt^{2+}+Pt^{4+})$ (%)
Pd/CZ	32	42	--
0.5Pd-0.5Pt/CZ	24	36	83
Pt/CZ	35	55	84

Unfortunately, XPS analysis of Pd oxidation states via the 3d core-level was not feasible for the Pd/CZ and 0.5Pd-0.5Pt/CZ catalysts due to significant spectral interference from Zr 3p orbitals. Specifically, the Pd $3d_{5/2}$ peak and Pd $3d_{3/2}$ peaks typically located at ~335.0 eV and ~340.0 eV, respectively, overlaps energetically with the Zr $3p_{3/2}$ (~330 eV) and Zr $3p_{1/2}$ peaks (~344 eV) signals [53]. This energetic overlap complicates peak deconvolution, making it challenging to reliably quantify the Pd oxidation states.

Structure–activity correlations

The results show that catalytic performance in H_2-SCR of NO is controlled by the balance between hydrogen activation and its selective utilization for NO reduction. Under the studied conditions, Pt/CZ promotes strong low-temperature activity but also favours rapid H_2 consumption, which limits N_2 selectivity. Pd/CZ provides a more favourable balance between activity and selectivity, indicating that metal identity plays a central role in controlling the competition between selective NO reduction and non-selective H_2 oxidation.

The bimetallic catalysts display a modified activity–selectivity balance rather than a simple enhancement of NO conversion. In particular, the delayed H_2 consumption and improved N_2 selectivity suggest that incorporating Pd and Pt within the same supported catalyst moderates hydrogen utilization and suppresses, to some extent, pathways leading to non-selective H_2 oxidation. The comparison with the physical mixture indicates that this behaviour cannot be fully reproduced by the simple coexistence of separate Pd- and Pt-containing catalyst particles. Instead, the H_2-TPR results indicate that co-impregnation produces a different reduction environment for the noble-metal species, exhibiting the presence of Pd-Pt interactions.

Further evidence of a modified Pd/Pt surface environment is provided by CO-DRIFTS. Whereas Pd/CZ exhibits CO adsorption features associated with contiguous Pd ensembles, these features are weakened and altered in the bimetallic catalyst. This indicates that the surface arrangement and/or electronic environment of Pd sites is modified by the presence of Pt. Such changes are consistent with disruption of contiguous Pd ensembles, electronic interaction between Pd and Pt, or the formation of Pt–Pd interfacial sites. Importantly, these observations support the presence of modified Pd/Pt surface environments but do not provide definitive evidence for the formation of a Pt–Pd alloy.

Overall, the catalytic behaviour of the bimetallic catalysts can be attributed to the combined influence of the intrinsic properties of Pd and Pt and the modified surface environment generated by co-impregnation on the CeO_2–ZrO_2 support. The interaction between these factors alters hydrogen activation and utilization, thereby shifting the balance between NO conversion and N_2 selectivity. Determining whether these modified sites correspond to alloyed particles, closely associated segregated domains, or specific Pt–Pd interfacial structures would require additional atomic-scale or operando characterization.

Open Access Article. Published on 08 June 2026. Downloaded on 6/8/2026 11:29:15 PM.
This article is licensed under a Creative Commons Attribution 3.0 Unported Licence.

Catalysis Science & Technology Accepted Manuscript

Please do not adjust margins

Conclusion

This study establishes the influence of noble-metal identity and Pd–Pt interactions on the H_2-SCR performance of CeO_2–ZrO_2-supported catalysts under lean conditions. Pt/CZ exhibited the highest low-temperature activity, reaching 98% NO conversion at 175 °C; however, its rapid H_2 consumption was accompanied by a pronounced decrease in N_2 selectivity. In contrast, Pd/CZ maintained high NO conversion over a broader low-temperature range while providing higher N_2 selectivity, indicating that Pd achieves a more favourable balance between hydrogen activation and selective NO reduction.

The incorporation of Pd and Pt into bimetallic catalysts modified this activity–selectivity relationship rather than simply increasing NO conversion. Among the bimetallic formulations, 0.7Pd–0.3Pt/CZ exhibited the highest NO conversion, whereas 0.5Pd–0.5Pt/CZ showed the most favourable selectivity behaviour, maintaining more than 75% N_2 selectivity between 150 and 350 °C. The delayed H_2 consumption observed for the bimetallic catalysts indicates a modification of hydrogen utilization, which appears to limit low-temperature conversion but contributes to suppressing non-selective H_2 oxidation and preserving N_2 selectivity over a wider temperature interval.

The comparison with the physical mixture demonstrated that the behaviour of the co-impregnated bimetallic catalyst cannot be reproduced simply by combining Pd/CZ and Pt/CZ in the reactor bed. H_2-TPR showed that co-impregnation modifies the reduction environment of the noble-metal species, while CO-DRIFTS revealed changes in the CO adsorption behaviour of Pd-containing surface sites in the presence of Pt. In particular, the modification of Pd-associated multi-coordinated CO features is consistent with disruption of contiguous Pd ensembles and/or the formation of modified Pd–Pt interfacial environments.

Author contributions

Baqer Aljaman: Conceptualization, Methodology, Data curation, Formal Analysis, Writing - Original draft, Writing - review & editing. **Sarah Komaty:** Methodology, Writing - review & editing. **Nawaf M Alghamdi:** Investigation, Project Administration, Funding Acquisition, Writing - review & editing. **Christos Kalamaras:** Investigation, Project Administration, Funding Acquisition, review & editing. **S. Mani Sarathy:** Supervision, Project Administration, Writing - review & editing**. Javier Ruiz-Martinez:** Supervision, Project Administration, Writing - review & editing.

Conflicts of interest

There are no conflicts to declare.

Data availability

The authors confirm that the data supporting the findings of this study are available within the article and its supplementary Information (SI).

View Article Online
DOI: 10.1039/D6CY00260A

Acknowledgements

The The authors acknowledge the financial support by Saudi Aramco under project #FuelCom4. The authors also thank Eganathan Kaliyamoorthy for assistance with ICP-OES measurements, Mark Meijerink for TEM measurements and Ildar Mukhambetov for technical support.

References

1 H. Ritchie, Sector by sector: where do global greenhouse gas emissions come from?, https://ourworldindata.org/ghg-emissions-by-sector, (accessed 3 November 2024).

2 P. Kamboj, M. Hejazi, Y. Qiu, P. Kyle and G. Iyer, *Energy Strategy Reviews*, DOI:10.1016/j.esr.2024.101537.

3 D. POPP, Euro 7: Deal on new EU rules to reduce road transport emissions, https://www.europarl.europa.eu/news/en/press-room/20231207IPR15740/euro-7-deal-on-new-eu-rules-to-reduce-road-transport-emissions, (accessed 22 March 2025).

4 E. M. Szumska and R. S. Jurecki, *Energies (Basel).*, DOI:10.3390/en14164821.

5 M. De Gennaro, E. Paffumi, G. Martini, U. Manfredi, H. Scholz, H. Lacher, H. Kuehnelt and D. Simic, in *SAE Technical Papers*, SAE International, 2014, vol. 1.

6 Z. Stępień, *MDPI*, 2021, preprint, DOI: 10.3390/en14206504.

7 *Nitrogen Oxides (NOx), Why and How They Are Controlled*, 1999.

8 L. Chen, S. Ren, L. Liu, B. Su, J. Yang, Z. Chen, M. Wang and Q. Liu, *J. Environ. Chem. Eng.*, DOI:10.1016/j.jece.2022.107167.

9 S. Komaty, M. Andijani, N. Wang, J. C. Navarro de Miguel, S. Kumar Veeranmaril, M. N. Hedhili, C. I. Q. Silva, Y. Wang, M. Abou-Daher, Y. Han and J. Ruiz-Martinez, *Environ. Sci. Technol.*, DOI:10.1021/acs.est.4c01585.

Open Access Article. Published on 08 June 2026. Downloaded on 6/8/2026 11:29:15 PM.
This article is licensed under a Creative Commons Attribution 3.0 Unported Licence.

Catalysis Science & Technology Accepted Manuscript

This journal is © The Royal Society of Chemistry 2026

Please do not adjust margins

View Article Online
DOI: 10.1039/D6CY00260A

10 R. Khairova, S. Komaty, A. Dikhtiarenko, J. L. Cerrillo, S. K. Veeranmaril, S. Telalović, A. A. Tapia, J. L. Hazemann, J. Ruiz-Martinez and J. Gascon, *Angew. Chem. Int. Ed.*, DOI:10.1002/anie.202311048.

11 P. M. More, D. L. Nguyen, P. Granger, C. Dujardin, M. K. Dongare and S. B. Umbarkar, *Appl. Catal. B*, 2015, **174–175**, 145–156.

12 P. S. Kim, M. K. Kim, B. K. Cho, I. S. Nam and S. H. Oh, *J. Catal.*, 2013, **301**, 65–76.

13 R. Mrad, A. Aissat, R. Cousin, D. Courcot and S. Siffert, *Appl. Catal. A Gen.*, 2015, **504**, 542–548.

14 G. G. Olympiou and A. M. Efstathiou, *Chemical Engineering Journal*, 2011, **170**, 424–432.

15 M. Leicht, F. J. P. Schott, M. Bruns and S. Kureti, *Appl. Catal. B*, 2012, **117–118**, 275–282.

16 A. Väliheikki, K. C. Petallidou, C. M. Kalamaras, T. Kolli, M. Huuhtanen, T. Maunula, R. L. Keiski and A. M. Efstathiou, *Appl. Catal. B*, 2014, **156–157**, 72–83.

17 C. Xu, W. Sun, L. Cao, T. Li, X. Cai and J. Yang, *Chemical Engineering Journal*, 2017, **308**, 980–987.

18 L. E. Gevers, L. R. Enakonda, A. Shahid, S. Ould-Chikh, C. I. Q. Silva, P. P. Paalanen, A. Aguilar-Tapia, J. L. Hazemann, M. N. Hedhili, F. Wen and J. Ruiz-Martínez, *Nat. Commun.*, DOI:10.1038/s41467-022-30679-9.

19 A. F. Suarez-Corredor, J. Shao, B. Westerberg, M. U. Bäbler and L. Olsson, *Applied Catalysis B: Environment and Energy*, 2026, **395**, 126855.

20 Y. Li, Y. Huang, H. Zhao, Y. Fan, J. Li, H. Xu, J. Wang and Y. Chen, *J. Colloid Interface Sci.*, 2025, **691**, 137443.

21 J. Shao, P. H. Ho, D. Creaser and L. Olsson, *Applied Catalysis O: Open*, 2024, **188**, 206947.

22 M. Jabłońska and A. Osorio Hernández, *John Wiley and Sons Inc*, 2024, preprint, DOI: 10.1002/cctc.202400977.

23 M. Maurer, R. Popescu, H. Störmer, M. Casapu and J.-D. Grunwaldt, *Applied Catalysis B: Environment and Energy*, 2026, **386**, 126347.

24 V. K. Patel and S. Sharma, *Catal. Today*, 2021, **375**, 591–600.

25 E. Aneggi, M. Boaro, S. Colussi, C. de Leitenburg and A. Trovarelli, in *Handbook on the Physics and Chemistry of Rare Earths*, Elsevier B.V., 2016, vol. 50, pp. 209–242.

26 C. M. Kalamaras, G. G. Olympiou, V. I. Pârvulescu, B. Cojocaru and A. M. Efstathiou, *Appl. Catal. B*, 2017, **206**, 308–318.

27 S. Xu, Z. Liu, C. Peng and Z. Liu, *ACS Appl. Nano Mater.*, DOI:10.1021/acsanm.4c07324.

28 Y. Zhang, S. Xu, J. Li, E. He and Z. Liu, *Journal of Physical Chemistry C*, 2023, **127**, 7248–7256.

29 Y. Li, Y. Huang, H. Zhao, Y. Fan, J. Li, H. Xu, J. Wang and Y. Chen, *J. Colloid Interface Sci.*, DOI:10.1016/j.jcis.2025.137443.

30 K. S. W. SING, D. H. EVERETT and R. A. W. HAUL, *INTERNATIONAL UNION OF PURE AND APPLIED CHEMISTRY PHYSICAL CHEMISTRY DIVISION COMMISSION ON COLLOID AND SURFACE CHEMISTRY INCLUDING CATALYSIS* REPORTING PHYSISORPTION DATA FOR GAS/SOLID SYSTEMS with Special Reference to the Determination of Surface Area and Porosity Reporting physisorption data for gas/solid systems-with special reference to the determination of surface area and porosity*, 1985.

31 F. Jonas, B. Lebeau, S. Siffert, L. Michelin, C. Poupin, R. Cousin, L. Josien, L. Vidal, M. Mallet, P. Gaudin and J. L. Blin, *ACS Appl. Nano Mater.*, 2021, **4**, 1786–1797.

Open Access Article. Published on 08 June 2026. Downloaded on 6/8/2026 11:29:15 PM.
This article is licensed under a Creative Commons Attribution 3.0 Unported Licence.

Catalysis Science & Technology Accepted Manuscript

Please do not adjust margins

View Article Online
DOI: 10.1039/D6CY00260A

32 S. N. Kabekkodu, A. Dosen and T. N. Blanton, *Powder Diffr.*, 2024, **39**, 47–59.

33 K. Chen, J. Wan, T. Wang, Q. Sun and R. Zhou, *Journal of Rare Earths*, 2023, **41**, 896–904.

34 M. Luo, F. Wang, Q. Liu, W. Li, C. Shao, X. Liu and B. Ai, *Reaction Kinetics, Mechanisms and Catalysis*, 2023, **136**, 2039–2051.

35 H. Wang, Y. Chen, Q. Zhang, Q. Zhu, M. Gong and M. Zhao, *Journal of Natural Gas Chemistry*, 2009, **18**, 211–216.

36 H. Zhang, J. Wang, Y. Zhang, Y. Jiao, C. Ren, M. Gong and Y. Chen, *Appl. Surf. Sci.*, 2016, **377**, 48–55.

37 C. Karakaya and O. Deutschmann, *Appl. Catal. A Gen.*, 2012, **445–446**, 221–230.

38 P. Canton, G. Fagherazzi, M. Battagliarin, F. Menegazzo, F. Pinna and N. Pernicone, *Langmuir*, 2002, **18**, 6530–6535.

39 H. Unterhalt, G. Rupprechter and H.-J. Freund, *J. Phys. Chem. B*, 2002, **106**, 356–367.

40 M. J. Hossain, M. M. Rahman and Md. Jafar Sharif, *Nanoscale Adv.*, 2020, **2**, 1245–1252.

41 D. S. Dolling, J. Chen, J.-C. Schober, M. Creutzburg, A. Jeromin, V. Vonk, D. I. Sharapa, T. F. Keller, P. N. Plessow, H. Noei and A. Stierle, *ACS Nano*, 2024, **18**, 31098–31108.

42 C. Li, Y. Sakata, T. Arai, K. Domen, K. Maruya and T. Onishi, *Journal of the Chemical Society, Faraday Transactions 1: Physical Chemistry in Condensed Phases*, 1989, **85**, 929–943.

43 K. Föttinger, W. Emhofer, D. Lennon and G. Rupprechter, *Top. Catal.*, 2017, **60**, 1722–1734.

44 X. Wu, L. Xu and D. Weng, *Appl. Surf. Sci.*, 2004, **221**, 375–383.

45 A. E. Nelson and K. H. Schulz, *Appl. Surf. Sci.*, 2003, **210**, 206–221.

46 F. Zhang, P. Wang, J. Koberstein, S. Khalid and S. W. Chan, *Surf. Sci.*, 2004, **563**, 74–82.

47 S. Ricote, G. Jacobs, M. Milling, Y. Ji, P. M. Patterson and B. H. Davis, *Appl. Catal. A Gen.*, 2006, **303**, 35–47.

48 C. N. Costa, A. M. Efstathiou, V. N. Stathopoulos and V. C. Belessi, *J. Catal.*, 2001, **197**, 350–364.

49 T. Nagasawa, A. Kobayashi, S. Sato, H. Kosaka, K. Kim, H. Min You, K. Hanamura, A. Terada and T. Mishima, *Chemical Engineering Journal*, DOI:10.1016/j.cej.2022.139937.

50 L. S. Kibis, D. A. Svintsitskiy, A. I. Stadnichenko, E. M. Slavinskaya, A. V. Romanenko, E. A. Fedorova, O. A. Stonkus, V. A. Svetlichnyi, E. D. Fakhrutdinova, M. Vorokhta, B. Šmíd, D. E. Doronkin, V. Marchuk, J. D. Grunwaldt and A. I. Boronin, *Catal. Sci. Technol.*, 2021, **11**, 250–263.

51 J. Lu, Y. Li, S. Li and S. P. Jiang, *Sci. Rep.*, DOI:10.1038/srep21530.

52 Q. Zhang, T. Chen, R. Jiang and F. Jiang, *RSC Adv.*, 2020, **10**, 10134–10143.

53 M. Zhao, H. Zhang, X. Li and Y. Chen, *Journal of Energy Chemistry*, 2014, **23**, 755–760.

Open Access Article. Published on 08 June 2026. Downloaded on 6/8/2026 11:29:15 PM.
This article is licensed under a Creative Commons Attribution 3.0 Unported Licence.

Catalysis Science & Technology Accepted Manuscript

This journal is © The Royal Society of Chemistry 2026

Please do not adjust margins

Data Availability Statement

View Article Online
DOI: 10.1039/D6CY00260A

The authors confirm that the data supporting the findings of this study are available within the article and its supplementary Information (SI).

Open Access Article. Published on 08 June 2026. Downloaded on 6/8/2026 11:29:15 PM.
This article is licensed under a Creative Commons Attribution 3.0 Unported Licence.

Catalysis Science & Technology Accepted Manuscript